Experiments and simulations of tunnel-ionized plasmas

W. P. Leemans,* C. E. Clayton, W. B. Mori, K. A. Marsh, P. K. Kaw,† A. Dyson, and C. Joshi
Electrical Engineering Department, University of California Los Angeles, Los Angeles, California 90024

J. M. Wallace
Los Alamos National Laboratory, Los Alamos, New Mexico 87545

The tunneling-ionization model predicts that fully ionized plasmas with controllable perpendicular ($T_\perp$) and negligible longitudinal temperature ($T_\parallel$) can be produced. The validity of these predictions has been studied through experiments and supporting theory and simulations. Emission of odd harmonics of the laser frequency, indicative of a stepwise ionization process, has been observed. X-ray measurements show that the plasma temperature is higher for a circularly polarized laser-produced plasma compared to when linear polarization is used. Analytically we find that the growth of the stimulated Raman (SRS) and Compton scattering (SCS) instabilities are suppressed during the ionization phase. A higher $T_\parallel$ than expected from the single-particle-tunneling model was observed after the ionization phase through SCS fluctuation spectra. The maximum achievable plasma density is found to be limited by ionization induced refraction. One-dimensional (1D) simulations show that, after the ionization phase, the initial $T_\parallel$ is low as expected from the single particle model and SRS density fluctuations grow to large values. In 2D simulations, however, $T_\parallel$ at the end of the ionization phase is already much higher and only SCS is seen to grow. The simulations indicate that stochastic heating and the Weibel instability play an important role in plasma heating in all directions and in making the plasma isotropic. Two-dimensional simulations also confirm that refraction plays a crucial role in determining the maximum electron density that can be obtained in such plasmas.

PACS number(s): 52.40.Nk, 52.50.Jm

I. INTRODUCTION

In this paper we explore the plasma-physics aspects of gases ionized via tunneling ionization through experiments and supporting particle-in-cell computer simulations. The continued increase in intensity of short-pulse lasers has opened the possibility of creating a dense plasma through tunneling ionization [1,2]. The electric field of a high-intensity laser can become on the order of the atomic field that binds an electron to the nucleus, allowing the laser to ionize the atom. In principle this optically induced ionization must be modeled taking into account the quantum nature of the atom and the time variation of fields. According to Keldysh's theory, however, in the limit where the Keldysh parameter $\kappa = (E_{ion}/2\Phi_p)^{1/2} \ll 1$, one can model the ionization as a process in which the electron tunnels through the suppressed Coulomb barrier of the nucleus, during a fraction of a single laser cycle. Here E_{ion} is the ionization potential and Φ_p the ponderomotive potential associated with the laser fields. The probability of tunneling through this suppressed barrier becomes significant when the electric field of the laser normalized to the atomic unit of the electric field is larger than about 0.01. Once the electron is free, it is assumed to start at rest and its subsequent motion can be determined by solving the equation of motion in the presence of plane-wave electromagnetic fields [3–5]. In the plane-wave limit, conservation of the canonical momentum requires that the velocity is composed of the electron quiver velocity v_{osc}

in the laser field and a drift velocity. The magnitude and direction of the drift velocity is dependent on the polarization of the ionizing laser, which suggests that for $\Phi_p/mc^2 \ll 1$ and $\kappa \ll 1$, plasmas with negligible longitudinal temperature $T_\parallel$ and controllable transverse temperature $T_\perp$ can be produced [5,6]. Here m is the electron mass and c the speed of light.

In a recent experiment, Corkum *et al.* have shown that in the single-particle regime and the long-wavelength (10.6-μm laser) regime the above description is indeed valid [5]. Although "tunneling ionization" of single atoms has been studied with both 10- and 1-μm laser pulses, most of the work on tunneling ionization of gases has been conducted in a very-low pressure gas, i.e., in the single-particle regime [5,7–9]. High-density plasma production using tunneling ionization has recently become of interest for x-ray recombination lasers [6,10] and plasma-based accelerators [11–13]. For an x-ray-recombination laser, plasmas need to be produced with densities n_e up to 10^{20} cm^{-3} and temperatures below 20 eV. In plasma-based-accelerator schemes it is desirable to have long regions of homogeneous plasma at fairly high densities (10^{16}–10^{18} cm^{-3}). In such dense plasmas space-charge effects cannot be neglected, thereby complicating a simple extrapolation of the single-particle results to predict the properties and behavior of macroscopic plasmas. Plasma-physics issues need to be considered in determining both the initial plasma characteristics and the evolution of such a plasma. It is our goal to see if the predictions of the tunneling-ionization model for a single

particle can be extrapolated to a space-charge-dominated plasma regime, and to address the plasma physics aspects of such tunnel-ionized plasma [14].

As shown in Fig. 1, we divide the interaction of an intense, short laser pulse with the gas target into four different phases. In the first phase the laser intensity is below the ionization threshold and hence no plasma will be produced. The intensity can, however, be high enough to generate harmonics of the laser frequency through the nonlinear polarizability of the gaseous target. This effect will be considered when analyzing the observed harmonic emission in the experiment. In the second phase, the ionization phase, the laser intensity has exceeded the ionization threshold and the gas becomes ionized. We calculate the time evolution of the plasma density and the electron distribution functions using the Keldysh model of tunneling ionization. In this model the electron tunnels through the suppressed Coulomb barrier of the nucleus and then interacts classically with the applied electromagnetic fields. The key predictions from this model are that a fully ionized plasma can be created with density controlled by the fill pressure and with an anisotropic electron-distribution function ($T_\perp$ larger than $T_\parallel$) controlled by the polarization of the ionizing laser. Furthermore, when using linear polarization, harmonics of the laser frequency could be generated through the stepwise-ionization process. A stepwise increase in plasma density is most pronounced when the laser intensity is slightly above threshold and ionization occurs only during a small part of a laser cycle. In this ionization phase, the laser-plasma parametric instabilities such as stimulated Raman scattering (SRS) and stimulated Compton scattering (SCS) are strongly affected by the rapidly varying plasma density and rapidly evolving anisotropic plasma temperature. Additionally, the maximum density of the plasma can be clamped due to beam refraction. Refraction occurs because the tunneling-ionization rate is exponentially dependent on the laser field and this leads to steep plasma-density gradients in the transverse or radial direction.

In the third phase, plasma-physics issues resulting from the continued interaction of the high-density laser beam with the space-charge-dominated plasma have to be considered. When electrons are created into nonplanar waves the electric fields have a longitudinal component (such as in the case of a focusing or a refracting beam), resulting in a longitudinal drift velocity or a high $T_\parallel$. Also, electrons created at the same longitudinal but different radial position will end up with a different drift velocity magnitude due to the fields radial dependence causing a smearing of the resulting distribution function. Furthermore, the electrons, retained by the space charge, keep interacting with the radial and longitudinal space-dependent electromagnetic fields. Both effects give rise to an effective stochastic heating [15].

As the plasma density saturates, the parametric instabilities can start growing during this second phase. For small $k\lambda_{De}$ (high plasma density, low $T_\parallel$), SRS can occur, while for large $k\lambda_{De}$, SCS can occur. Here k is the wave number of the density fluctuation and λ_{De} is the plasma Debye length. At the same time the anisotropic distribution function will relax due to instabilities such as the Weibel instability [16], causing a continued increase of $T_\parallel$, which in turn influences the evolution of SRS and SCS. On even longer time scales stimulated Brillouin scattering (SBS) will grow and hydrodynamic effects such as plasma expansion and/or ponderomotive blow out will become important.

In the fourth and final phase, the laser intensity drops below the threshold for the parametric instabilities, but the isotropization due to the Weibel instability and the plasma expansion can continue. Eventually the plasma will recombine.

In this paper we describe some of the first experiments that explore the physics issues unique to tunnel-ionized plasmas as discussed above. In Sec. II theoretical considerations relevant to the understanding of the experiment are discussed. In Sec. III experimental results are presented and in Sec. IV simulation results are shown which have been used to explain the experimental results.

II. THEORETICAL CONSIDERATIONS

A. Tunneling-ionization model

The characteristics of a plasma produced through ionization of a gas by an intense laser are calculated using the tunneling model [1]. First we calculate the plasma-density evolution during the ionization phase and then we calculate the resulting electron-distribution functions at the end of the ionization phase. In tunneling ionization, the rate at which the plasma density increases is given, for singly ionized gases, by

$$\frac{dn(t)}{dt} = w(t)[n_0 - n(t)] , \qquad (1)$$

where $n(t)$ is the time-dependent electron plasma density, n_0 is the initial neutral gas density, and $w(t)$ is given by [1]

$$w(t) = \frac{4me^4}{\hbar^3}\left[\frac{E_i}{E_H}\right]^{5/2}\zeta\exp\left[-\frac{2}{3}\left[\frac{E_i}{E_H}\right]^{3/2}\zeta\right] . \qquad (2)$$
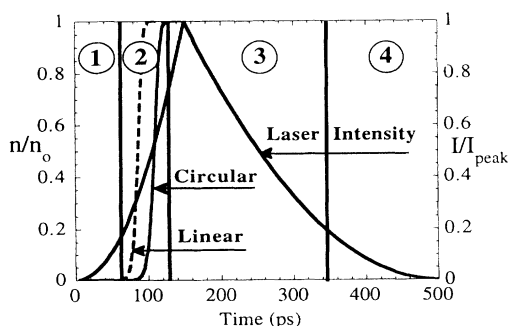
FIG. 1. Calculated evolution of the plasma density (normalized to the neutral gas fill density) as a function of time for a linearly (dashed line) and circularly (solid line) polarized laser shot into argon gas. No plasma effects were taken into account. The laser pulse had a 150-ps rise time and a 350-ps fall time and a peak intensity of 2×10^{14} W/cm². The four different phases in the interaction of a high-intensity laser beam with a gas considered in the paper are denoted by the point-dash lines.

Here E_H and E_i are the ionization potential of hydrogen, the atom in question, $\zeta = E_a/E(t)$ where $E_a = m^2 e^5/\hbar^4 \approx 5.21 \times 10^{11}$ V/m, is the atomic unit of electric field, and $E(t)$ is the amplitude of the applied electric field; e is the electron charge and ω_0 is the laser frequency. In the "plasma regime" we expect that a small fraction of electrons will leave the focal volume and build up a space-charge potential. A simple estimate, based on Gauss's law, shows that the space-charge potential reaches a large enough value to confine the bulk of the remaining electrons when a charge imbalance δn exists larger than

$$\delta n = \frac{\Phi_p}{2\pi e^2 \sigma^2} . \qquad (3)$$

Here σ is the radius of the plasma cylinder, defined as the position where the laser intensity is at its threshold value for ionization. For our experimental parameters δn needs to exceed 10^{12} cm^{-3} for space charge to retain the electrons. The rate equation for the plasma density has been verified experimentally and found to adequately model the time evolution of the plasma density [17].

As an example, using a CO_2 laser with a peak intensity of 3×10^{14} W/cm^2 and pulse rise time of 150 ps focused in hydrogen gas, we find from Eq. (1) that the density builds up rapidly in about 20 ps once the laser intensity exceeds 6×10^{13} W/cm^2. For a given intensity, the ionization onset occurs later with circular than with linear polarization, since the field strength is $\sqrt{2}$ lower (Fig. 1).

In the absence of plasma effects, the evolution of the electron energy distribution can be calculated assuming classical interaction of the newly created electrons with the ionizing electromagnetic fields [3,5]. Assuming that the electron is created at rest in a specific phase of the electric field, $\mathbf{E} = E \sin\omega_0 t\, \mathbf{y} + \alpha E \cos\omega_0 t\, \mathbf{z}$, it can be shown that its energy in the laser field is comprised of the quiver energy

$$E_{osc} = \frac{1}{2} m v_{osc}^2 = \frac{1}{2} \frac{e^2 E^2 \cos^2\omega_0 t}{m \omega_0^2} , \qquad (4)$$

plus translational drift energy

$$E_{trans} = m \frac{v_y^2 + \alpha v_z^2}{2} . \qquad (5)$$

The laser propagates in the x direction, v_y, and v_z are the dc drift-velocity components in the transverse y and z directions, respectively, and α is the degree of ellipticity of the incident polarization. This drift velocity arises because the transverse canonical momentum of the electron in a plane wave is a constant of the motion. This model has been shown to predict the correct values of laser-polarization-dependent anisotropic drift-energy distributions in an experiment in the single-atom regime by Corkum et al. [5]. One-dimensional (1D) calculations using the ionization probability from Eq. (2) and the energies from Eq. (5) show that for the previously considered laser parameters and using circularly polarized light, a ring distribution with a major radius (transverse to the incident laser-beam wave vector $\mathbf{k}_0$) of 2.5 keV and a minor radius of 1 keV with $T_{\parallel}$ of only 4 eV is generated upon

completion of ionization. This is shown in Figs. 2(a)–2(c). When using linearly polarized light an anisotropic quasi-Maxwellian with $T_{\perp} \approx 150$ eV and $T_{\parallel} \ll 1$ eV is produced for linearly polarized light. This is shown in Fig. 2(d). To summarize, from the tunneling-ionization model one expects that when the laser intensity is above the tunneling threshold but $v_{osc}/c < 1$, fully ionized plasmas with controllable $T_{\perp}$ and negligible $T_{\parallel}$ can be produced.

B. Stimulated Raman scattering in a time-varying plasma

In the experiment, coherent Thomson scattering of SRS- and/or SCS-driven high-frequency density fluctuations is used to provide information on the evolution of the plasma density and temperature. In a seminal paper by Rosenbluth, the theory of three-wave parametric instabilities for weakly inhomogeneous media was derived [18]. Following a similar analysis we consider the effect of time-varying plasma conditions on the growth of electron-density fluctuations excited through stimulated Raman or Compton scattering. The time dependence comes about through ionization and/or plasma heating. First we will analyze Raman scattering in a cold plasma with a time-dependent density and/or pump strength. Next we will include the effect of a time-dependent temperature for the case of Compton scattering.

Let $\mathbf{E}_0(\omega_0, k_0)$ be the pump wave, $\mathbf{E}_1(\omega_1, k_1)$ the scattered electromagnetic wave, and $\mathbf{E}(\omega, k)$ the electrostatic plasma wave. The plasma density n is assumed to be spatially uniform but to vary as a function of time. In the case of tunneling ionization the rate at which n changes is given by Eq. (1), whereas for collisional ionization

$$\frac{dn}{dt} = \lambda n (N - n) = \lambda n N \left[1 - \frac{n}{N} \right] . \qquad (6)$$
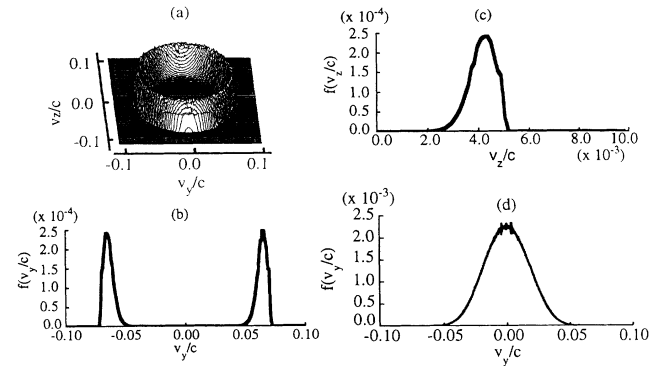

FIG. 2. (a) The calculated (single-particle regime) 2D transverse-electron drift-velocity distribution $f(v_y, v_z)$ produced by a circularly polarized laser with an intensity of 1.2×10^{14} W/cm^2, in argon gas. (b) Slice through (a) at $v_z = 0$, showing a major radius of $0.065c$ and a minor radius of $0.006c$. (c) Associated longitudinal drift-velocity distribution (10 times expanded velocity scale). (d) Calculated (single-particle regime) transverse-electron drift-velocity distribution $f(v_y)$ produced by a linear polarized laser with an intensity of 1.2×10^{14} W/cm^2, in argon gas. This quasi-Maxwellian distribution has a temperature $T_{\perp}$ of about 150 eV. The longitudinal drift-velocity distribution (not shown) is also quasi-Maxwellian with $T_{\parallel} \ll 1$ eV.

The continuity equation is modified for an ionizing plasma through the addition of a source term $S(t)$:

$$\frac{\partial n}{\partial t} + \nabla \cdot (n\mathbf{v}) = S(t) , \tag{7}$$

where $S(t)$ is equal to the ionization rate. Denoting the fluctuating density by $\tilde{n}(t)$ we write the density as $n(t) = n_0(t) + \tilde{n}(t)$, where $n_0(t)$ is the time-dependent background electron density. Since the rate of plasma production due to tunneling ionization only depends on the available amount of neutral species $N - n(t)$, there is no change in the equation of continuity for the fluctuations. However, for collisional ionization the rate is proportional to the amount of free electrons. If there is an electron-density fluctuation present in the plasma it would imply that at local-density maxima a higher ionization rate could enhance the density fluctuations. For a propagating fluctuation, however, this local enhancement smears out and since the newly created electrons do not oscillate, the wave is actually damped. The equation of continuity for $\tilde{n}$ is then

$$\partial_t \tilde{n} + n_0 \nabla \cdot \tilde{\mathbf{v}} = 0 , \tag{8}$$

where we have left out the explicit time dependence in the notation. The equation of motion of the density fluctuations is modified by the tunneling ionization through the addition of a damping term [19]

$$\partial_t \mathbf{v} + \frac{e}{m}\mathbf{E} = -\nabla(\mathbf{v}_0 \cdot \mathbf{v}_1^*) + \lambda \left[1 - \frac{N}{n_0} \right] \mathbf{v} . \tag{9}$$

Taking the divergence of Eq. (9), the time derivative of the continuity equation, and using Gauss's law

$$\nabla \cdot \mathbf{E} = -4\pi \tilde{n} e , \tag{10}$$

we obtain

$$\partial_t^2 \tilde{n} + \nu \partial_t \tilde{n} + \omega_p^2(t)\tilde{n} = n_0 \nabla^2(\mathbf{v}_0 \cdot \mathbf{v}_1^*) \tag{11}$$

describing the driven density fluctuations in an ionizing plasma. Here ν is the sum of a phenomenological damping rate and the damping rate due to ionization found in Eq. (9),

$$\mathbf{v}_j = \frac{e\mathbf{E}_j}{m\omega_j} \quad (j = 0, 1) , \tag{12}$$

where $\mathbf{E}_0$ is the applied electromagnetic field at frequency ω_0 and $\mathbf{E}_1$ is the backscattered electromagnetic field at frequency ω_1. From Maxwell's equations we can also derive the equation governing the behavior of the scattered e.m. wave:

$$(\partial_t^2 + c^2\nabla^2 + \omega_p^2)\mathbf{E}_1 = -\omega_p^2 \tilde{n}^* \mathbf{E}_0 , \tag{13}$$

where we have assumed that the electrons are created at rest. We now write

$$\tilde{n} = \hat{n} \exp \left[i\left[kx - \int \omega \, dt \right] \right] ,$$

$$\mathbf{E}_0 = \hat{E}_0 \exp \left[i\left[k_0 x - \int \omega_0 dt \right] \right] \mathbf{e}_0 , \tag{14}$$

$$\mathbf{E}_1 = \hat{E}_1 \exp \left[i\left[k_1 x - \int \omega_1 dt \right] \right] \mathbf{e}_1 ,$$

and will assume that $\hat{n}$, $\hat{E}_0$, and $\hat{E}_1$ are slowly varying amplitudes, i.e.,

$$\partial_t^2 \hat{n} \ll \omega \partial_t \hat{n} \tag{15}$$

and

$$\partial_t^2 \hat{E}_j \ll \omega \partial_t \hat{E}_j \quad \text{where } j = 0, 1 .$$

Applying the Fourier transform in space and using Eq. (15), we can rewrite the coupled Eqs. (11) and (13) in the slowly-varying-envelope approximation:

$$(\nu - 2i\omega)\partial_t \hat{n} - i\omega\nu\hat{n} = -\frac{e^2 k^2 \hat{E}_0}{m\omega_0\omega_1}n_0\hat{E}_1^* \exp \left[-i\int \Delta\omega \, dt \right]$$

$$= -A\hat{E}_1^* \exp \left[-i\int \Delta\omega \, dt \right] , \tag{16a}$$

$$(\nu_1 + 2i\omega_1)\partial_t \hat{E}_1^* + i\omega_1\nu_1\hat{E}_1^* = -\omega_p^2 \hat{n}\hat{E}_0^* \exp \left[i\int \Delta\omega \, dt \right] . \tag{16b}$$

Here ν_1 is a phenomenological damping rate of the electromagnetic wave, $\Delta\omega = \omega_0 - \omega_1 - \omega$, and $A = e^2 k^2 \hat{E}_0/m\omega_0\omega_1 n_0$. Since the plasma is assumed to be homogeneous, there is no wave-vector mismatch, i.e., $\Delta k = k_0 - k_1 - k = 0$. Eliminating E^* from Eqs. (16a) and (16b), we obtain the following equation for $\hat{n}$:

$$\partial_t^2 \hat{n} + \partial_t \hat{n} \left[i\Delta\omega - \frac{\dot{A}}{A} - \frac{i\omega\nu}{\nu - 2i\omega} + \frac{i\omega_1\nu_1}{\nu_1 + 2i\omega_1} + \frac{\dot{\nu} - 2i\dot{\omega}}{\nu - 2i\omega} \right]$$

$$+ \hat{n} \left[\frac{(\Delta\omega + i\dot{A}/A)\omega\nu}{\nu - 2i\omega} + \frac{\omega\omega_1\nu\nu_1 - \Gamma_0^2}{(\nu_1 + 2i\omega_1)(\nu - 2i\omega)} \right.$$

$$\left. - \frac{(\dot{\omega}\nu + \omega\dot{\nu})}{\nu - 2i\omega} \right] = 0 , \tag{17}$$

where $\Gamma_0^2 = A\omega_p^2 \hat{E}_0^* = (e^2 k^2 E_0^2/m\omega_0\omega_1)\omega_p^2$. Here Γ_0 is the homogeneous growth rate for the time-independent case [20] and the time derivative of A and ω is denoted by an overdot. Let $\overline{\Delta\omega} = \Delta\omega + i(\dot{A}/A)$, $\overline{\nu}_1/2 = \nu_1/2 + \dot{\omega}/\omega$, $\nu_{\text{eff}} = \nu/2 + \overline{\nu}_1/2$, and $\gamma_0^2 = \Gamma_0^2/4\omega\omega_1$. Assume $\nu \ll \omega_1, \omega$, then we can rewrite Eq. (14) as

$$\partial_t^2 \hat{n} + \partial_t \hat{n}[i\overline{\Delta\omega} + \nu_{\text{eff}}] + \hat{n} \left[i\frac{\overline{\Delta\omega}\nu}{2} + \frac{\nu\overline{\nu}_1}{2} - \gamma_0^2 \right] = 0 . \tag{18}$$

Using

$$\hat{n} = n' \exp \left[-\frac{1}{2}\int (i\overline{\Delta\omega} + \nu_{\text{eff}})dt \right] , \tag{19}$$

Eq. (18) can be reduced to

$$\partial_t^2 n' + n' \left[-\frac{i}{2}\overline{\Delta\omega} - \frac{1}{4}\left[i\overline{\Delta\omega} + \frac{\overline{\nu}_1 - \nu}{2} \right]^2 - \gamma_0^2 \right] = 0 . \tag{20}$$

In general, the detuning $\Delta\omega$ can be a complicated function of time. The rate at which the frequencies of the electromagnetic waves change in time is given by $d\omega_j/dt = (\omega_p/\omega_j)(d\omega_p/dt)$ where $j = 0, 1$, and therefore

can be neglected for an underdense plasma. It follows that

$$\frac{d\Delta\omega}{dt} = \frac{d\omega_0}{dt} - \frac{d\omega_1}{dt} - \frac{d\omega}{dt} \approx -\frac{d\omega_p}{dt} \, , \qquad (21)$$

where ω approximately equals ω_p. To this point we have been completely general in allowing for time dependence of both E_0 and n_0. In what follows we neglect the time dependence of E_0 (i.e., A), because for our experiment the ionization time is much shorter than the laser-pulse rise time. However, for ultrashort pulses this may not be the case. To obtain an analytic expression for the amplification of the density fluctuations due to Raman scattering, we now linearize the detuning $\Delta\omega$ in time around the point where $\Delta\omega=0$, i.e., $\Delta\omega=-Bt$. Using Eq. (21) this implies that the density is assumed to increase quadratically with time around $t=0$. We next assume that the pump strength varies on a slower time scale than the density and that the effective damping v_1-v is small. Normalizing time to $t=t'/B^{1/2}$, Eq. (20) becomes

$$\partial_{t'}^2 n' + \frac{t'^2}{4} n' + \left[\frac{i}{2} - \frac{\gamma_0^2}{B} \right] n' = 0 \, . \qquad (22)$$

An approximate solution for $\gamma_0^2/B > 0$ is then

$$n' = n_0' \sinh \int_{-t_c}^{t_c} \left[\frac{\gamma_0^2}{B} - \frac{t'^2}{4} \right]^{1/2} dt' \, , \qquad (23)$$

where we have neglected i in Eq. (22), since we assume finite amplification larger than 1. The integration is carried out to the turning points $t_c = 2\gamma_0/\sqrt{B}$. The net amplification is then

$$K = \int_{-t_c}^{t_c} \left[\frac{\gamma_0^2}{B} - \frac{t'^2}{4} \right]^{1/2} dt' = \pi \frac{\gamma_0^2}{B} \qquad (24)$$

and hence

$$n' = n_0' \exp \left[\pi \frac{\gamma_0^2}{B} \right] \qquad (25)$$

or

$$n = n_0' \exp \left[\pi \frac{\gamma_0^2}{B} - \frac{\gamma_0}{B} v_1 \right] \, . \qquad (26)$$

The effect of the time-dependent density is therefore equivalent to reducing the effective growth rate of SRS to $\gamma_{\text{eff}} = \gamma_0/\sqrt{B}$ and allowing growth only during a time roughly equal to the turning-point time $\Delta t = 2\gamma_0/\sqrt{B}$.

C. Stimulated compton scattering in a time-dependent plasma

To model stimulated Compton scattering in a plasma with a time-dependent density due to tunneling ionization, we start from the Vlasov equation with a source term

$$\frac{\partial f}{\partial t} + \mathbf{v} \cdot \nabla f - \left[\frac{e}{m} \mathbf{E} + \frac{\nabla \mathbf{v}_0 \cdot \mathbf{v}_1^*}{m} \right] \cdot \frac{\partial f}{\partial \mathbf{v}} = S(\mathbf{v}, t) \, , \qquad (27)$$

where

$$S(\mathbf{v}, t) = w(t)(N_0 - n)\delta(\mathbf{v}) \, . \qquad (28)$$

The use of $\delta(\mathbf{v})$ explicitly demands new electrons to be created at rest. The time evolution of the zeroth-order distribution function is then determined by

$$\frac{\partial f_0}{\partial t} = -w(t)n_0 \left[1 - \frac{N_0}{n_0} \right] \delta(\mathbf{v}) \qquad (29)$$

and the first-order perturbation f_1 satisfies the equation

$$\frac{\partial f_1}{\partial t} + i\mathbf{k} \cdot \mathbf{v} f_1 - \left[\frac{e}{m} \mathbf{E} + i\mathbf{k} \frac{\mathbf{v}_0 \cdot \mathbf{v}_1^*}{m} \right] \cdot \frac{\partial f_0}{\partial \mathbf{v}} = 0 \, . \qquad (30)$$

Letting

$$f_1 = \tilde{f}_1 \exp \left[ikx - i \int \omega \, dt \right] \, ,$$

$$n_1 = \tilde{n}_1 \exp \left[ikx - i \int \omega \, dt \right] \, , \qquad (31)$$

and applying a spatial and temporal Fourier transform to Eq. (30), we obtain

$$\tilde{f}_1 = i \left[\frac{e}{m} \mathbf{E} + i\mathbf{k} \frac{\mathbf{v}_0 \cdot \mathbf{v}_1^*}{m} \right] \cdot \frac{\partial f_0/\partial \mathbf{v}}{\omega - kv_x} \qquad (32)$$

and, integrating with respect to v, we find the fluctuating density n_1 to be given by

$$n_1 = i \frac{ke}{km} \cdot \left[\mathbf{E} + \frac{i}{e} \mathbf{k} \cdot (\mathbf{v}_0 \cdot \mathbf{v}_1^*) \right] \int \frac{\partial f_0/\partial v}{\omega - kv_x} d^3v \, . \qquad (33)$$

We now define the plasma susceptibility χ_e as

$$\chi_e = \frac{4\pi e^2}{km} \int \frac{\partial_v f_0}{\omega - kv_x} dv \, . \qquad (34)$$

The time dependence of both the density and temperature are contained in the expression for χ_e through its dependence on f_0. Fourier transforming Gauss's law [Eq. (10)] we get

$$n_1 = -i \frac{\mathbf{k} \cdot \mathbf{E}}{4\pi e} \, . \qquad (35)$$

Using Eqs. (10), (34), and (35) we can rewrite Eq. (33) as

$$n_1 = -\frac{\chi_e}{1 + \chi_e} E_0 A_1 E_1^* \, . \qquad (36)$$

In the weakly damped limit Eq. (16a) can be rewritten as

$$\partial_t E_1^* + \frac{v_1}{2} E_1^* = i n_1 E_1^* = i n_1 E_0^* A_2 \, . \qquad (37)$$

Finally, combining Eqs. (36) and (37) and integrating with respect to time we obtain

$$E_1^* = E_{10}^* \exp \left[-\int \left[\frac{v_1}{2} - i E_0^2 A_1 A_2 \frac{\chi_e}{1 + \chi_e} \right] dt \right] \, . \qquad (38)$$

The density fluctuations will therefore have an amplification factor given by

$$\exp\left\{\int\left[A_1 A_2 E_0^2 \mathrm{Im}\left[\frac{\chi_e}{1+\chi_e}\right]-\frac{\nu_1}{2}\right]dt\right\} . \qquad (39)$$

The integration has to be carried out up to a time which is the shorter of the laser pulse length τ_{pulse} and the time it takes for the light wave to convect from the location of the source (usually right-hand boundary of the plasma) to the location of the observer. The convection velocity for the Compton waves can be neglected, since these waves are heavily damped.

If the plasma conditions and pump are time independent, then Eq. (39) reduces to the usual time-independent Compton growth rate [20] given by

$$\gamma_c = 2\left[\frac{\nu_0}{c}\right]^2 \omega_0 \mathrm{Im}\frac{\chi_e(\omega,k\lambda_{\mathrm{De}})}{1+\chi_e(\omega,k\lambda_{\mathrm{De}})} . \qquad (40)$$

The associated spatial growth rate is then given by

$$\kappa_c = 2\left[\frac{\nu_0}{c}\right]^2 \frac{\omega_0}{c}\mathrm{Im}\frac{\chi_e(\omega,k\lambda_{\mathrm{De}})}{1+\chi_e(\omega,k\lambda_{\mathrm{De}})} , \qquad (41)$$

where the group velocity of the light wave is assumed to be c (underdense plasma).

D. Ionization-induced refraction

Because the ionization rate [Eq. (2)] has a strong non-linear dependence on the applied field, a plasma with strong radial density gradients is formed when a Gaussian transverse laser-intensity profile is used. This plasma can then act as a negative lens and refract the laser beam, causing the intensity to clamp close to the ionization threshold thereby suppressing further ionization [21].

A simple estimate for the scale lengths associated with refraction can be obtained as follows. In an inhomogeneous medium, one can calculate the path taken by a light ray from the paraxial ray equation

$$d\theta = \frac{\partial \Delta\eta}{\partial r}ds , \qquad (42)$$

where $\Delta\eta = \eta_{\mathrm{vac}} - \eta_{\mathrm{med}}$ and η_{vac} and η_{med}, the index of refraction of vacuum and the medium, respectively. The index of refraction for electromagnetic waves in an underdense plasma can be approximated as

$$\eta_p = \frac{ck}{\omega} = (1-\omega_p^2/\omega^2)^{1/2} \approx 1-\frac{1}{2}\frac{n(r)}{n_c} , \qquad (43)$$

where n_c is the critical density and $n(r)$ is the radial density profile. Substituting Eq. (43) into Eq. (42) we obtain

$$d\theta = \frac{1}{2}\frac{\partial n/n_c}{\partial r}ds . \qquad (44)$$

The total bending angle after traveling a distance L is given by

$$\theta = \frac{1}{2}\int\frac{\partial(n/n_c)}{\partial r}ds$$

and scales as

$$\frac{1}{2}\frac{L}{L_D}\frac{z_0}{w_0}\frac{n}{n_c} , \qquad (45)$$

where L_D is the density gradient scale length normalized to the beam size at the waist w_0, and L is the path length normalized to the Rayleigh range $z_0 = \pi w_0^2/\lambda$, with λ the wavelength of the laser.

We next derive a scaling law for intensity clamping due to refraction for pulses longer than the Rayleigh length, by incorporating the paraxial ray equation into Gaussian beam optics. Initially, as the laser intensity increases above the ionization threshold, plasma will be produced in a small volume. Subsequent light rays entering the plasma and converging towards the focus will now be bent due to refraction. If the slope of the rays is zero at the location where the laser intensity is just below threshold, then further ionization will be prevented and the plasma density will cease to increase.

The intensity profile for a Gaussian beam is given by

$$I(s,\rho)=I_{\mathrm{peak}}\frac{\exp[-2(\rho/\nu)^2]}{\nu^2} , \qquad (46)$$

where

$$\nu(s)=\frac{w(s)}{w_0}=(1+s^2)^{1/2}, \quad s=z/z_0, \quad \rho=\frac{r}{w_0} , \qquad (47)$$

with I_{peak} the peak laser intensity. The rate at which the intensity changes as a function of s is given by

$$\frac{\partial I(s,\rho)}{\partial s} = -2I_{\mathrm{peak}}\frac{\exp[-2(\rho/\nu)^2]}{\nu^3}[1-2(\rho/\nu)^2]\frac{d\nu}{ds} \qquad (48)$$

and

$$\left[\frac{d\nu}{ds}\right]_{\mathrm{Gauss}} = \frac{s}{(1+s^2)^{1/2}} . \qquad (49)$$

Geometrically, $(d\nu/ds)_{\mathrm{Gauss}}$ is just the beam convergence (for $s<0$) or expansion $(s>0)$ angle due to Gaussian focusing. Refraction is going to change the spot size by an amount

$$\left[\frac{d\nu}{ds}\right]_{\mathrm{refrac}} = \frac{z_0}{w_0}d\theta = \frac{1}{2}\left[\frac{z_0}{w_0}\right]^2\frac{\partial(n/n_c)}{\partial\rho}ds . \qquad (50)$$

Therefore the total rate of change of the spot size is proportional to

$$\left[\frac{d\nu}{ds}\right]_{\mathrm{total}} \equiv \left[\frac{d\nu}{ds}\right]_{\mathrm{Gauss}} + \left[\frac{d\nu}{ds}\right]_{\mathrm{refrac}} . \qquad (51)$$

The intensity remains constant, or reduces, when $(d\nu/ds)_{\mathrm{total}} \geq 0$, which gives

$$n/n_c ds \geq 2\left[\frac{w_0}{z_0}\right]^2\frac{sL_D}{(1+s^2)^{1/2}} , \qquad (52)$$

where ds is the path length in the plasma. Ionization will be suppressed if the rate of beam size change is larger than zero at a location $s=s_{\mathrm{thresh}}$, where the intensity reaches the ionization threshold. In the absence of re-

fraction, s_{thresh} is obtained from Eq. (46) (setting $\rho = 0$) and Eq. (47):

$$s_{thresh} = \sqrt{\Psi - 1} \tag{53}$$

with $\Psi = I_{peak}/I_{thresh}$. The radial density-gradient scale length is roughly set by the width of the ionization threshold intensity contour. To find the maximum width of the ionization threshold contour we rewrite Eq. (46) as

$$\rho = v \left[\frac{1}{2}\ln\left[\frac{\Psi}{v^2} \right] \right]^{1/2} \tag{54}$$

and take the derivative with respect to s:

$$\frac{\partial \rho}{\partial s} = \frac{\partial v}{\partial s} \left\{ \left[\frac{1}{2}\ln\left[\frac{\psi}{v^2} \right] \right]^{1/2} - \frac{1}{\left[\frac{1}{2}\ln\left[\frac{\psi}{v^2} \right] \right]^{1/2}} \right\} = 0 . \tag{55}$$

Equation (55) is satisfied when $\partial v /\partial s = 0$, which is true for $s = 0$, i.e., the beam waist location, or when $\frac{1}{2}\ln(\Psi/v^2) = 1$, which implies $v = \sqrt{\Psi}/e$. Therefore a second extremum occurs when $\sqrt{\Psi} > e$. At this transition point the Gaussian contours for the ionization threshold change from oval to dumbbell shape. The radial scale length L_D is then given by $L_D = \sqrt{\frac{1}{2}\ln\Psi}$ for $\Psi < e^2$ and $L_D = \sqrt{\Psi}/e$ for $\Psi > e^2$. Equation (52) then becomes

$$n/n_c ds \geq 2 \left[\frac{w_0}{z_0} \right]^2 \left[\frac{\Psi - 1}{2\Psi}\ln\Psi \right]^{1/2} \quad \text{for } \Psi < e^2 \tag{56}$$

and

$$n/n_c ds \geq 2 \left[\frac{w_0}{z_0} \right]^2 \left[\frac{\Psi - 1}{e^2} \right]^{1/2} \quad \text{for } \Psi > e^2 . \tag{57}$$

To estimate the path length ds after which refraction competes with the focusing of the beam, we used a simple 2D code to calculate the density profile produced through ionization by a traveling laser pulse. The ionization rate is given by Eqs. (1) and (2). The spatial beam profile is prescribed by Gaussian optics and remains unchanged in the calculation. In Fig. 3(a) the density contours are shown for the case of a CO_2 pulse ($I_{peak} = 1.2 \times 10^{14}$ W/cm^2) shot into hydrogen gas with $c\tau_{pulse}/z_0 \approx 12$. In Fig. 3(b) the density contours (one quadrant) are shown for a Nd:YAG (where YAG denotes yttrium aluminum garnet) laser shot into helium gas ($I_{peak} = 2 \times 10^{17}$ W/cm^2) with $c\tau_{pulse}/z_0 \approx 0.28$. It is found that for the CO_2 case, the plasma size is on the order of z_0, while for the Nd:YAG case, it is $16 z_0$. In order for the intensity to be below the ionization threshold at the vacuum focus, the plasma needs to be dense enough along a path length of roughly $\frac{1}{4}$ the size of the plasma. Therefore, taking ds to be on the order of $(s_{thresh}/2)z_0$, we finally obtain an estimate for the maximum plasma density in the presence of ionization-induced refraction
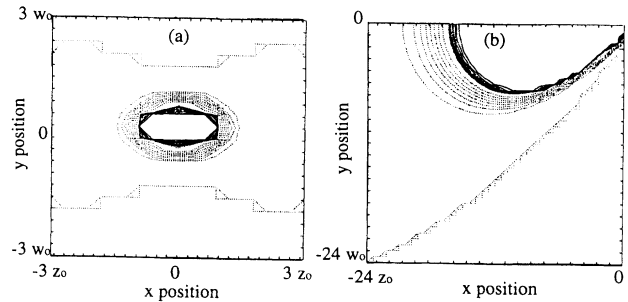

FIG. 3. (a) Plasma-density contours for a CO_2-laser-($I_{peak} = 1.2 \times 10^{14}$ W/cm^2) produced plasma. The box goes from $-3z_0$ to $3z_0$ in the horizontal direction and from $-3w_0$ to $3w_0$ in the vertical direction. The highest density contour is 1 (normalized to the neutral-gas density). The dashed contours increase by 10% while the solid contours increase by 1%. The total plasma length with $n/n_0 = 1$ is approximately z_0; (b) Plasma-density contours for a YAG-laser- ($I_{peak} = 2 \times 10^{17}$ W/cm^2) produced plasma (one quadrant). The box goes from $-24z_0$ to 0 in the horizontal direction and from $-24w_0$ to 0 in the vertical direction. The highest density contour is 1 (normalized to the neutral gas density). The dashed contours increase by 10% while the solid contours increase by 1%. The total plasma length at $n/n_0 = 1$ is approximately $16z_0$.

$$n/n_c \leq \frac{4\lambda}{\pi z_0} \left[\frac{\ln\Psi}{2\Psi} \right]^{1/2} \quad \text{for } \Psi < e^2 \tag{58}$$

and

$$n/n_c \leq \frac{4\lambda}{\pi e z_0} \quad \text{for } \Psi > e^2 . \tag{59}$$

From this analysis it is clear that refraction-induced density clamping can be avoided in two ways: (a) by using a high-intensity pulse with effective pulse length shorter than the "refraction length" and (b) by reducing the length of gas through which the laser has to propagate when using a laser with a spatial pulse length $c\tau_{pulse}$ long compared to the Rayleigh range.

III. EXPERIMENT

In the experiment, a CO_2-laser beam (up to 100-J, 150-ps rise time and 350-ps fall time) was focused into a vacuum chamber containing up to 5 Torr of Ar or H_2 gas. The measured spot size in vacuum was $2w_0 = 340$ μm and the peak laser intensity in vacuum was around 3×10^{14} W/cm^2. At this intensity, an estimate based on Eq. (3) shows that, for fill pressures exceeding 1 mTorr, the space-charge potential is large enough to confine most of the electrons against the ponderomotive potential of the laser. The space-charge-dominated plasma was produced over approximately two Rayleigh lengths, $2z_0 = 1.7$ cm. Since the laser pulse has a full width at half maximum (FWHM) of about 350 ps, $c\tau_{pulse}/z_0 \approx 12$. The plasma was diagnosed by (a) viewing the forward laser harmonic emission; (b) collective Thomson scattering of a 0.5-μm beam to probe $2k_0$ density fluctuations; and (c) by measuring the x-ray emission from the plasma. Using the

tunneling-ionization rate equation [Eq. (1)] and neglecting any pump depletion, we found that in Ar gas full ionization (to $Z=1$) is attained for our experimental parameters in approximately 25 ps once the ionization threshold of 6×10^{13} W/cm² is exceeded. As in the case of single atoms [7], no significant plasma formation was detected either visually or on any of the above diagnostics, below an average laser intensity of 6×10^{13} W/cm². Above this threshold, both line and continuum emission were observed but always in the recombination phase of the plasma, almost 5 ns after the laser pulse was over. This supports the notion that collisional excitation and ionization are relatively unimportant in our work.

A. Harmonic generation

The evidence for plasma formation by tunneling comes from odd-harmonic emission from the plasma. When linear polarization is used the ionization proceeds in stepwise fashion at twice the laser frequency generating a nonlinear current $J(l\omega_0, lk_0) = -evn_e$, $l = 3, 5, 7, \ldots$ which acts as a source term for odd harmonic emission [22]. The frequency spectrum of the transmitted or forward-scattered laser light was measured through bandpass filters. The energy in the second harmonic and third harmonic was measured using a spectrograph and pyro-array detector combination allowing a direct measurement of the linewidth of the radiation. The spectrum was found to contain discrete lines at the second ($\Delta\lambda/\lambda < 10^{-3}$) and third ($\Delta\lambda/\lambda < 10^{-3}$) harmonic. Moreover, a signal at the fifth-harmonic wavelength was observed through bandpass filters and the use of a spectrograph and a liquid-helium-cooled Ge:Cu detector [Fig. 4(a)]. In Fig. 4(b) the harmonic signal level as a function of the ellipticity α is plotted for the second and the third harmonic. As expected from the tunneling mechanism, the third and the fifth harmonic (not plotted) were found to decrease in magnitude as the ellipticity of the beam α was increased. The second harmonic signal, however, was found to be independent of polarization.

Since the harmonic infrared emission was not time resolved, we can only put an upper bound on the pulse length $\tau_{3\omega}$ when we convert the measured amount of energy into peak pulse power. If the harmonics were generated by the tunneling mechanism they will only be emitted during the ionization phase, i.e., $\tau_{3\omega} \approx 25$ ps. The maximum theoretical efficiency P_{2r+1}/P_I is given by [22]

$$\frac{P_{2r+1}}{P_1} = \frac{12 \left[\dfrac{\omega_a}{\omega_L}\right]^2 \zeta \exp\left[-\dfrac{4}{3}\zeta\right]}{\pi r^4 (2r+1)^2}$$

$$\times \left\{ \exp\left[\frac{-3r^2}{\zeta}\right] \right.$$

$$\left. + \frac{r}{r+1}\exp\left[-3\frac{(r+1)^2}{\zeta}\right] \right\}^2 D , \quad (60)$$

where $2r+1$ is the order of the harmonic. Here D is the detuning factor for a collimated beam given by

$$D = \frac{\sin^2(\Delta k L/2)}{(\Delta k L/2)^2} , \quad (61)$$

where L is the length of the medium and Δk is the wavevector mismatch between fundamental and third harmonic given by [22]

$$\Delta k = -rk_0 \frac{\omega_p^2}{\omega_0^2} = -rk_0 \frac{n}{n_c} . \quad (62)$$

The value for ζ is calculated using the laser field strength at the moment where the density is half its final value and equals about 18. For our experimental parameters $n/n_c \approx 10^{-3}$, $L \approx 1$ cm, and $k_0 = 5.9 \times 10^3$ cm^{-1} so that $D \approx 3.5 \times 10^{-3}$. The theoretical ratio P_3/P_1 is then a factor of about 5 above the measured value of 5×10^{-8}, but the difference may be due to the uncertainty in $\tau_{3\omega}$ and in D. The theoretical ratio P_5/P_3 is about $\frac{1}{120}$, which is reasonably close to the experimental ratio of about $\frac{1}{160}$.

In addition to stepwise ionization, odd harmonics can be generated through the nonlinear susceptibility $\chi^{(3)}$ of the media [23] through which the laser beam propagates and through relativistic effects inside the plasma [24]. Harmonic emission due to the $\chi^{(3)}$ process will follow the laser pulse, while relativistic effects can only be important close to the peak of the pulse. The background signal level, with the chamber evacuated, can indeed be accounted for by nonlinear processes in the NaCl windows
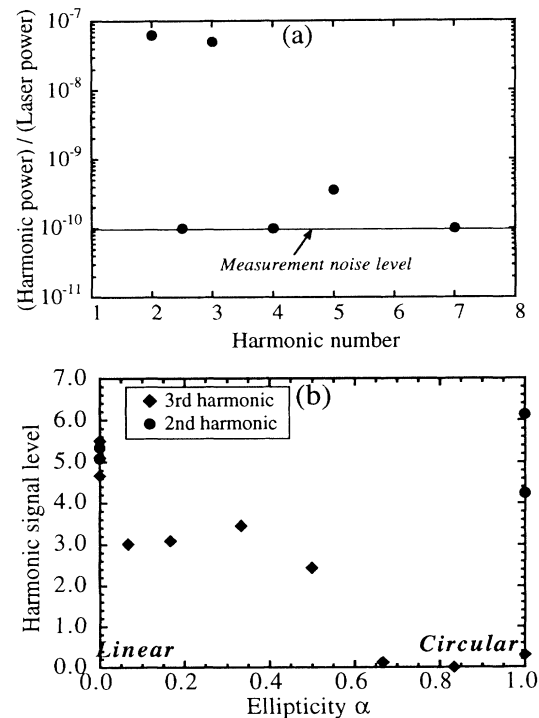

FIG. 4. (a) Ratio of harmonic power to laser power for different harmonic numbers. To convert the measured amount of energy into power we have assumed the light to be emitted in a 25-ps-long pulse for all the different harmonics. (b) Measured second- and third-harmonic signal level as a function of the ellipticity α of the polarization of the ionizing laser beam.

and SF_6 gas [25], which is used to suppress self-lasing. Although the beam traverses neutral gas inside the target chamber, it is well known that no third harmonic will be generated for a strongly focusing beam when the medium is infinitely long [23]. When the nonlinear medium is finite in length (but still much longer than the Rayleigh range) and extends symmetrically on both ends of best focus, the ratio P_3/P_1 is given by [26]

$$\frac{P_3}{P_1} = \frac{\omega_3^2 |\chi^{(3)}|^2}{3^{3/2} n_3 n_1^3 c^4 \varepsilon_0^2} I_1^2 D .$$ (63)

Here $\chi^{(3)}$ is the nonlinear third-order susceptibility of the medium; n_1 and n_3 are the index of refraction of the medium at the fundamental and third harmonic, respectively; ω_3 is the frequency of the third harmonic; $b = 2z_0$ is the confocal parameter; z_b is the offset of the center of the nonlinear medium with respect to the Gaussian beam-waist position ($z=0$); and I_1 is the peak laser intensity. The detuning factor D for a Gaussian beam is given by [26]

$$D = \left| \int_0^L \frac{1}{\left[1+i2\dfrac{(z_b+z)}{b}\right]^2} \exp(-i\Delta kz)dz \right|^2 .$$ (64)

From Eq. (64) it is then found that $\chi^{(3)}$ effects are only becoming important when the Rayleigh range is longer than the length of the nonlinear medium (e.g., in a gas-jet experiment).

The magnitude of $\chi^{(3)}$ was measured in argon gas at relatively low laser intensity ($I \leq 10^{11}$ W/cm^2) using a 1.06-μm YAG laser, and atmospheric pressures [26]. To first order, $\chi^{(3)}$ and the indices of refraction n_1, n_3 can be extrapolated to other wavelengths and pressures using the relations given by Lehmeier et al. [26]. Since the laser enters the experiment as a collimated (i.e., Rayleigh range much longer than L), low-intensity ($I < 10^{11}$ W/cm^2) beam before being focused, the contribution to the third-harmonic signal along this path is given by Eq. (62), where the detuning factor D is given by Eq. (61). For our experimental parameters we then obtain $P_3/P_1 = 1.04 \times 10^{-19}$ and $P_3/P_1 = 1.53 \times 10^{-13}$ as contributions of the high-intensity focusing beam and the collimated beam, respectively. Here we have taken a neutral argon gas density of 1.8×10^{16} atoms/cm^3 and a fundamental power P_1 of 100 GW. Even if we assume the harmonic emission to occur for the entire laser pulse, i.e., $\tau_{\text{pulse}} = 500$ ps, it is clear from Fig. 4(a) that the measured third-harmonic efficiency is about five orders of magnitude larger than the theoretical contribution to harmonic generation due to $\chi^{(3)}$ in the neutral gas. Thus it seems unlikely that this mechanism can account for the observed harmonic emission.

Relativistic effects are also unimportant for the parameter regime of this experiment. The ratio of the third harmonic to the fundamental can be shown to be [27]

$$\frac{P_3}{P_1} = \left[\frac{9}{256}\right]^2 \left[\frac{\omega_p}{\omega_0}\right]^4 a_0^4 \left[1+\frac{a_0^2}{2}\right]^{-3} .$$ (65)

Here a_0 is equal to v_{osc}/c. In the experiment, the peak value of a_0 and the plasma density were 0.1 and $10^{-3} n_c$, respectively. The calculated efficiency is then more than six orders of magnitude below the measured level. Furthermore, the theoretical power ratio of the fifth to the third harmonic scales like third to fundamental. This is in even larger discrepancy with the measured efficiency for the fifth harmonic. In summary, both the nonlinear polarizability and the relativistic effects are therefore relatively unimportant in our experiment.

The second-harmonic emission observed in the experiment was found to be nearly independent of polarization, but cannot be explained by any of the above mechanisms. Simulations show that the second-harmonic emission originates from the edges of the plasma, where the density gradients are the steepest, suggesting that the source for the even harmonics are nonlinear currents due to transverse intensity or density gradients [28].

B. Time-resolved Thomson scattering

Our main density and $T_\parallel$ diagnostic is based on the detection of electron-density fluctuations with $k_p = 2k_0$ excited by the laser beam through either SRS [29] or SCS [30]. If the tunnel plasmas have very low values of $T_\parallel$, as the single-particle model suggests, then $k\lambda_{\text{De}} \ll 1$ and SRS should have a very large growth rate, whereas for large $T_\parallel$ and $k\lambda_{\text{De}}$ on the order of 1, SCS may occur. The scattered light from $2k_0$ density fluctuations was wavelength (0.2-Å resolution) and time resolved (10-ps resolution) with a spectrograph–streak-camera combination. However, it is not possible to follow the time evolution of the ionization process using this technique since the ionization rate is comparable to the homogeneous, time-independent growth rate for the Raman-Compton instability [20]. In Sec. II it was found that the homogeneous growth rate for SRS γ_0 is effectively reduced to $\gamma_{\text{eff}} = \gamma_0/\sqrt{B}$ and that the growth time is limited by the smaller of the convection time or the "detuning time" $\Delta t = 2\gamma_0/\sqrt{B}$. Here B is the rate with which the plasma frequency varies as a function of time. For our experimental conditions, the SRS amplification factor for thermal density fluctuations equals about two "e foldings" of gain, so that the Thomson-scattered signal remains below our detection threshold during the ionization phase.

Experiments show that the high-frequency $2k_0$ density fluctuations have a broad frequency spectrum consistent with Compton rather than Raman scattering. The evolution of one such spectrum from a plasma produced in a static fill of 1.1 Torr of H_2-gas is depicted in Figs. 5 and 6(a). At early times [Fig. 6(a)], the spectrum can be fitted quite well applying the stimulated Compton scattering theory [20,30]. In this second phase of the interaction of the laser with the plasma, we assume that the density and temperature are evolving on a slow enough time scale justifying the use of the time-independent growth rate for the stimulated Compton scattering instability. Furthermore, the driven fluctuations are assumed to grow from thermal noise. The scattered power in the noise spectrum $P_N(\omega, t=0)$ is given approximately by [31]
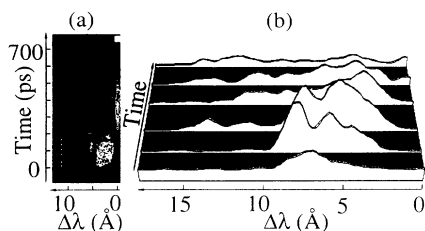
FIG. 5. (a) Streak camera image of the Thomson-scattered probe beam in a hydrogen plasma. The fill pressure was 1.1 Torr. Although not shown here, there was no blue shifted spectral feature visible in the original data. The white bar at the top indicates the location of a 100× attenuator for SBS. (b) Line outs of the streak data taken along the direction of the arrows in (a).

$$P_N(\omega,t=0)=Cn_e\left[\left|1-\frac{\chi_e}{\varepsilon}\right|^2 f_e\left[\frac{\omega}{k}\right]\right.$$
$$\left.+\left|\frac{\chi_e}{\varepsilon}\right|^2 f_i\left[\frac{\omega}{k}\right]\right],\qquad(66)$$

where ω is the frequency shift of the scattered light, $\varepsilon=(1+\chi_e)$, $f_e(f_i)$ is the electron (ion) velocity distribution function, and C is a constant dependent upon geometrical factors. The spatial growth rate $\kappa_C(\omega,k\lambda_{De})$ for backscattering modes with $\mathbf{k}\approx 2\mathbf{k}_0$ is given by Eq. (41). Equation (41) is valid away from the strongly coupled regime (i.e., $\kappa_C \ll \omega_p/c$), which, for our densities and laser intensities at early times during the interaction, is satisfied [20,32]. Also, since the SCS fluctuations propagate in a direction normal to the incident laser electric
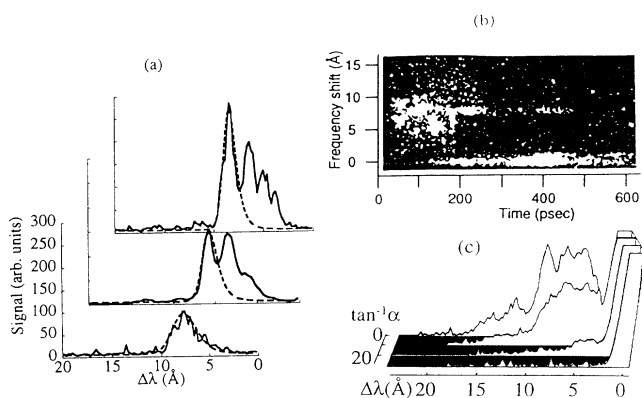

FIG. 6. (a) Plot of first three line outs and fitted curves; (b) time-resolved frequency spectrum of $2\mathbf{k}_0$ electron-density fluctuations. Wavelength shift increases upwards and time increases to the right. The feature near zero shift is from ion waves. The electron plasma wave feature due to SCS ranges from 0–15 Å. The feature at around 8 Å is the beat wave response of the plasma. The laser beam contained both a 10.3 and a 10.6-μm line, requiring a resonant density of 8×10^{15} cm^{-3}. (c) Time integrated streak camera images of the Thomson-scattered probe beam in hydrogen plasmas (fill pressure of 1.1 Torr) for different degrees of ellipticity α of the laser polarization ($\tan^{-1}\alpha=45$ for circular polarization).

field, i.e., $\mathbf{k}\cdot\mathbf{v}_0=0$, the expression for $\chi_e(\Delta\omega,k\lambda_{De})$ is thought not to be affected for the case where $v_0>v_e$, where $v_e=(KT_e/m)^{1/2}$ is the electron thermal velocity [33]. The scattered CO_2 power $P_s(\omega,L)$ is given by $P_s(\omega,L)=P_N\exp(\kappa L)$, where L is the length of the convective amplifier. Since the Thomson-scattering probe measures the density fluctuations associated with the CO_2 laser backscatter at one point in space z', the spectrum is then of the form

$$P_{TS}(\omega,t)=SP_N(\omega,k\lambda_{De},t=0)\exp[\kappa(\omega,k\lambda_{De})ct\,]$$

$$\text{for } t<T \qquad (67a)$$

$$=SP_N(\omega,k\lambda_{De},t=0)\exp[\kappa(\omega,k\lambda_{De})cT\,]$$

$$\text{for } t>T\,,\qquad(67b)$$

where we have assumed the group velocity of the light wave to be c for the underdense plasmas, T is the transit time of the scattered wave to the point z', and S is a fitting parameter. The effect of increasing $k\lambda_{De}$ beyond about 0.3 in Eqs. (67a) and (67b) is to significantly broaden the range of frequency shifts ω which have significant growth, leading to scattered spectra with widths becoming on the order of the maximum shift. In the fitting procedure we adjust $k\lambda_{De}$ and the plasma density so that both the position of the peak and the width of the main spectral feature of the calculated spectrum agrees with the experimental data. The parameters S and v_{osc}/c are adjusted so that the calculated and measured amplitudes of the background noise level and the main spectral feature agree.

Fitting the theoretical spectrum to the first line-out from Fig. 6(a) gives $n\approx 3.5-6\times10^{15}$ cm^{-3} and $T_\parallel\approx40-75$ eV, the higher temperature correlating with the lower density. This temperature is already much higher and the density much lower than predicted by the single-particle model. At later times the spectrum develops structure and broadens to both higher and lower frequencies. Applying the same fitting procedure at these times does not result in a good fit to the data [Fig. 6(a)]. About 140 ps after the onset of SCS, the spectrum resembles incoherent Thomson scattering from a thermal plasma rather than from a collective mode. These are still driven fluctuations as evidenced from the absence of scattered light on the blue side. The spectra possibly have evolved into the strongly coupled regime due to a decreasing plasma density caused by thermal expansion and/or ponderomotive blowout. This issue, however, clearly needs further theoretical attention. The most probable cause of the frequency broadening of the spectrum is a continued increase of $T_\parallel$. As will be seen later, this is believed to be due to the Weibel instability.

Even at higher fill pressures, the SCS spectra indicated very low peak densities with $n\le10^{-3}n_c$. At these low densities, collisional processes should be relatively unimportant on the time scales of the laser pulse. Also, at the higher pressures a significant amount of the laser energy was found to be refracted out of the original cone angle of the laser beam. We take this as evidence of density clamping due to ionization-induced refraction. This

prevents the laser intensity from being significantly above the ionization threshold for a sufficient duration to fully ionize the gas. This will be discussed in more detail in Sec. III D.

As an independent density diagnostic, we have also attempted to excite a plasma wave using a laser beam containing two different frequencies [13]. This process is known as beat-wave excitation [34,11] and relies on the fact that if the difference frequency of the two laser lines is close to the plasma frequency, a plasma wave will be resonantly excited. When the CO_2 laser was made to oscillate simultaneously on a 10.6- and a 10.3-μm line, requiring a plasma density on the order of 8×10^{15} cm^3, a signature of the long-wavelength plasma wave mode-coupled to an SBS-excited ion wave [35] was seen on the Thomson-scattering diagnostic [Fig. 6(b)]. However, when using the line pair 10.6 μm-9.6 μm, which requires a plasma density of 1.2×10^{17} cm^{-3}, this feature was never seen. This confirms independently that the density is much lower than 10^{17} cm^{-3}.

We also explored the possibility of laser-plasma instability control by varying the polarization of the laser beam. The main effect of changing the laser polarization is to drastically alter the initial transverse distribution of electron energies. If these distributions isotropize rapidly then $k\lambda_{De}$, and therefore the damping rate for high-frequency electron fluctuations, can be varied. As we increased α the fluctuations due to SBS were unaffected, whereas the high-frequency fluctuations became weaker and were eventually completely suppressed for $\alpha \geq 0.6$ [Fig. 6(c)]. These observations are consistent with an increase in $T_{\parallel}$ in going from linear to circularly polarized light. However, the inferred values for $T_{\parallel}$ are still anomalously higher than the single-particle predictions.

C. X-ray emission

To obtain an independent estimate of the plasma temperature and to explore the possibility of plasma temperature control through polarization of the ionizing laser light, soft-x-ray emission above 800 eV was measured using a silicon surface-barrier detector with Be and Mylar filters. Figure 7(c) shows three sets of data: linear polarization with the detector looking (i) along and (ii) transverse to the electric field, and (iii) circular polarization. A significant difference in x-ray flux was seen between linear and circular polarization, as expected from the tunnel-ionization model. However, no significant difference was seen between looking transverse to and along the electric field for the linear polarization.

To model the x-ray data we have measured that the x-rays are emitted by an isotropized Maxwellian, for both linear and circular polarization. The spectral distribution of the bremsstrahlung intensity from a Maxwellian distribution is given by [36]

$$S(\omega) = nS_0 e^{-\hbar\omega/k_B T} G \tag{68}$$

with

$$nS_0 = \frac{n_+ nZ^2}{m^2 c^3} \left[\frac{e^2}{4\pi\varepsilon_0} \right]^3 \frac{16}{3} \left[\frac{2\pi m}{3k_B T} \right]^{1/2} \tag{69}$$
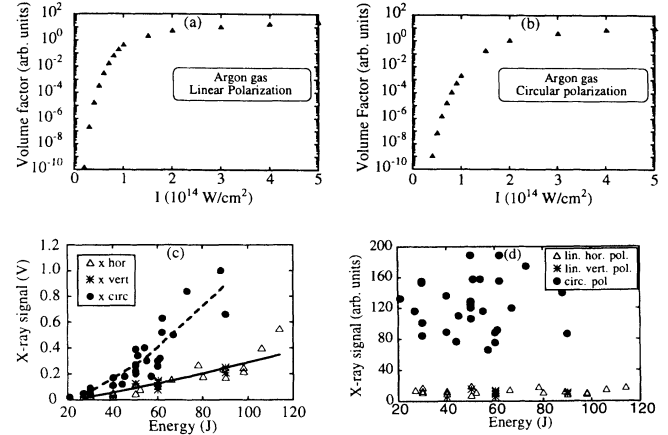

FIG. 7. Calculated volume factor as a function of laser intensity for calculating x-ray yield from an argon plasma produced with a (a) linearly and a (b) circularly polarized beam. (c) The x-ray emission from argon plasma (fill pressure of 280 mTorr) as a function of laser energy for different polarizations. (d) x-ray yield from (c) adjusted for the volume factor as a function of laser energy for linear polarization (detector looking horizontally and vertically) and circular polarization.

and G is the Maxwell-averaged Gaunt factor. The increase of x-ray flux with laser energy can simply be attributed to the increase of plasma volume at higher laser intensity. As seen from Eq. (69) the x-ray emission is proportional to the amount of ions and electrons. Using a 2D numerical ionization code we calculated the amount of electrons and ions produced through ionization for different laser intensities. The result is shown in Figs. 7(a) and 7(b). Taking this factor into account for the experimental data we found the x-ray signal to become roughly independent of laser energy as shown in Fig. 7(d). The spread in the data for circular polarization is mainly due to the uncertainty in the peak laser intensity. Since the exact pulse shape varies from shot to shot and a low-intensity pedestal can be present, an uncertainty in the peak laser intensity is introduced when converting the measured energy to power. As seen in Fig. 7(b) the slope of the volume factor curve for circular polarization is very steep in the range of $1-2 \times 10^{14}$ W/cm^2, thereby magnifying the uncertainty in the x-ray yield.

The bremsstrahlung spectrum from a Maxwellian plasma, with T as parameter, is then multiplied by the filter transmission spectra and the detector sensitivity curve. Integrating the resulting spectra gives the total amount of energy captured by the SSB detector. Experimentally we measured the x-ray flux through two different filter combinations (25-μm Be only and 25-μm Be plus 6.3-μm Mylar foil), keeping the laser energy and gas pressure constant. From the ratio of the x-ray yield for the two filters we obtain a plasma temperature for circular polarization of around 450±150 eV. Plasmas produced with a linearly polarized laser produced on average ten times less signal (taking the volume factor into account), so that their temperature is typically about 180±50 eV. These temperatures are within a factor of two of the $T_{\perp}$'s that might be expected from a laser beam which has its intensity

clamped close to the ionization threshold due to refraction.

D. Ionization-induced refraction

The clamping of the maximum density due to refraction was investigated by measuring the amount of laser light outside the original cone angle of the beam, as a function of fill pressure [Fig. 8(a)]. In Ar, as the fill pressure was raised beyond 200 mT, a sudden onset of refraction was seen. This corresponds to a density of around 0.7×10^{16} cm^{-3}. In H$_2$, refraction was found to be a more gradual function of pressure. On the laser-pulse time scale the Ar ions are relatively immobile and the radial density gradients are "frozen in," whereas in H$^+$ plasmas the ions can radially move during the laser pulse and relax the density gradients and thus reduce the defocusing. This conjecture was supported by the observation that the refraction effects could be reduced by using circularly polarized light (presumably higher $T_\perp$) instead of linearly polarized light [Fig. 8(b)].

In the experiment the ratio Ψ of laser intensity to threshold intensity was varied from 2 to 5, $2z_0 = 1.7$ cm, and $2w_0 = 340$ μm. Using Eq. (56) we obtain $n/n_c ds \geq 3 \times 10^{-4}$ (6.4×10^{-4}) for $\Psi = 2$ (5). From the density scaling law [Eq. (58)] we find that the maximum obtainable density for our experimental conditions is below $6.3 \times 10^{-4} n_c$, which is in good agreement with the experimental observations.
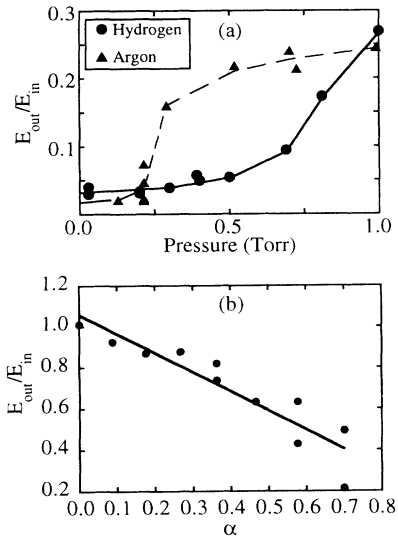

FIG. 8. (a) Ratio of the laser energy refracted outside of the original cone angle of the beam to the incident laser energy, in H$_2$ and Ar plasmas, as a function of neutral gas fill pressure for linearly polarized light. (b) Ratio of the laser energy refracted outside of the original cone angle of the beam to the incident laser energy, in H$_2$ plasmas, as a function of the ellipticity α of the polarization. The pressure was kept constant at 1.2 Torr. The energies are measured by two cross-calibrated calorimeters. The saturation of the refracted energy at 30% of the incident laser energy is consistent with the solid angle of detection of the calorimeter measuring the refracted beam energy.

IV. SIMULATIONS OF TUNNEL-IONIZED PLASMAS

A. Refraction

Ionization-induced beam refraction in tunneling-ionization produced plasmas was simulated using the two-dimensional particle-in-cell code WAVE [37]. The results were compared to the scaling laws obtained in Sec. II D.

The simulations were done on a grid of $200c/\omega_0$ along and $125c/\omega_0$ transverse to the laser propagation direction. All frequencies were normalized to the laser frequency of a 10.6-μm CO$_2$ laser. A neutral gas density of $0.1n_c$ was chosen and only singly ionized ions were allowed. The ionization rate in Eq. (2) was used and electrons were added with an initial thermal velocity (v_x, v_y, v_z) of $10^{-5}c$ (essentially at rest). The laser electric fields was S polarized (z direction) and launched from the left-hand boundary. The curvature of the phase fronts was given by

$$R(z) = (z - z_a)\left[1 + \left[\frac{z_0}{z - z_a}\right]^2\right], \qquad (70)$$

and z_a was chosen such that in vacuum the beam was focused in the middle of the simulation box (i.e., $x = 100c/\omega_0$). The laser pulse had a rise time of $750\omega_0^{-1}$ and a fall time of $1250\omega_0^{-1}$. The contour plot of the E_z field for a vacuum test run is shown in Fig. 9(a). Beam refraction is illustrated in Figs. 9(b) and 9(c), where the E_z-field contours and the plasma-density contours are shown at $T = 900\omega_0^{-1}$. With plasma the contour of
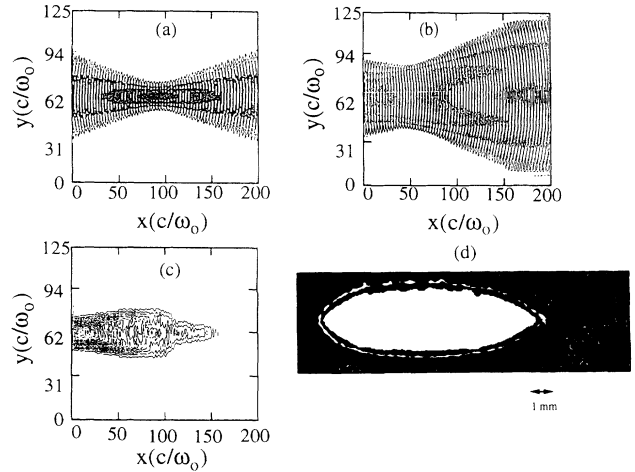

FIG. 9. (a) and (b) Calculated contour plots of E_z field and (c) of the plasma density from WAVE simulation at time step $T = 900\omega_0^{-1}$. The simulation box is $(200c/\omega_0 \times 125c/\omega_0)$. The incident laser field is launched from the left-hand boundary into vacuum in (a) and into a plasma with peak density $n = 0.1n_c$. In case (b) strong field refraction has occurred as seen from the E field peaking of axis at $x = 150c/\omega_0$ and the plane of highest intensity having moved backwards. Notice also in (c) how the location of the plasma is not centered on the box. (d) CCD camera image of the visible radiation given off by the plasma. The scale lengths in the experiment are different than in the simulation.

highest intensity has moved backwards, the minimum waist is wider, and the plasma is formed closer to the left-hand side of the simulation box. The formation of a ring-shaped beam profile is consistent with the experimental observation that, in the strong refraction regime, a significant amount (> 30%) of the beam energy is measured to be outside the original cone angle of the beam. Furthermore, a 2D image [Fig. 9(d)] of the visible radiation given off by the plasma when strong refraction occurs is remarkably similar to that of a plot of plasma-density contours obtained from the simulations [Fig. 9(c)], including the formation of a narrow region of plasma just to the right of the focus.

As seen in Figs. 9(a)–9(c), rays entering the simulation box at $y = 72c/\omega_0$ (edge of plasma) make an angle of about 0.22 rad; the radial density-gradient scale length is approximately $10c/\omega_0$ and the peak density is $0.1n_c$. From Eq. (45) we then find that the ray propagates parallel to the axes after a distance $L \approx 44c/\omega_0$, which agrees remarkably well with the simulation.

To verify the scaling law for the density clamping due to refraction we carried out a simulation in which the laser intensity was chosen so that according to Eq. (58) the density should stay below $0.9n_0$, where n_0 is the neutral gas density. When the simulation was run it was found that the maximum obtained density was $0.92n_0$, which is in good agreement with the predicted value.

B. Stochastic heating

To understand the origin of the initial $T_\parallel$ and its further increase with time, 2D simulations were carried out. In all cases a circularly polarized beam was launched from the left-hand boundary with a peak $v_{osc}/c = 0.1$. Ionization in linearly polarized beams leads to artificially large electron temperatures due to numerical phase errors. When a new electron and ion are created they are injected with an isotropic velocity of $10^{-5}c$.

As a check we compared the electron-distribution functions obtained from the simulations and from the analytic model for extremely low densities, $n/n_c = 10^{-8}$. They were found to be in excellent agreement [Figs. 10(a) and 10(b)]. Simulations with a fully ionized density of $10^{-2}n_c$ and a laser rise time of $750\omega_0^{-1}$ were done to isolate the high-frequency instabilities (SRS and/or SCS). In 1D, SRS was seen to grow to large levels ($\delta n/n = 0.3$) because of a very low initial $T_\parallel$ ($k\lambda_{De} \ll 1$), and saturate due to particle trapping. The incident and backscattered ω spectrum is shown in Fig. 11(a).

In 2D, however, where the beam was focused into the middle of the simulation box, SRS was suppressed because $T_\parallel$ at the end of the ionization was already large. Instead, SCS occurred at a reduced level, consistent with experimental observations. This is shown in Fig. 11(b).

This high $T_\parallel$ at the end of the ionization phase may have the following origins: (a) the electrons are created with a longitudinal drift-velocity component; (b) even when created with only a transverse drift-velocity component, electrons require a longitudinal drift-velocity through subsequent interaction with the electromagnetic fields. For the former case, electrons can be created at
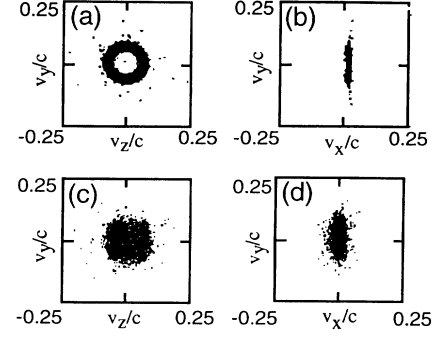

FIG. 10. Transverse (v_y, v_z) and longitudinal (v_y, v_x) velocity space without [(a) and (b)] and with "plasma" effects [(c) and (d)]. In (a) and (b) the simulation was done on a 1D grid. The maximum density was $n/n_c = 10^{-8}$. The laser rise and fall time was $500\omega_0^{-1}$. The major (minor) radius of the ring corresponds to a "temperature" of 1 keV (20 eV). In (c) and (d) the simulation was done on a 2D grid ($200c/\omega_0 \times 125c/\omega_0$). The peak density was $4 \times 10^{-4}n_c$. The laser beam was collimated and had a Gaussian transverse profile with a beam diameter of $30c/\omega_0$. The peak field strength corresponded to $0.1 \, v_{osc}/c$ for both the 1D and 2D simulations. The transverse (longitudinal) temperature at $T = 1200\omega_0^{-1}$ is ≈ 500 eV (50 eV).

positions where electric fields, for small-f-number focusing and/or strong refraction, have a substantial longitudinal component. This in turn results in a significant longitudinal drift-velocity component (i.e., $T_\parallel$) of the electrons. The variation of the field strength will result in broadening of the drift-velocity distribution, since particles born at different radial locations will end up with a different drift velocity. In the latter case the electrons, retained by the ion space charge, continue to interact with both the applied electromagnetic fields and the
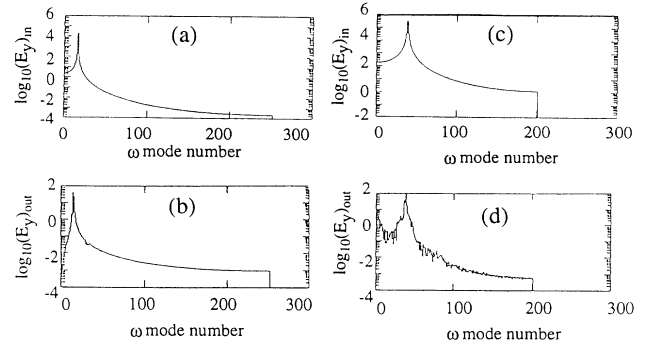

FIG. 11. (a) ω spectrum at the left-hand boundary of the incident electric-field component E_y for a 1D simulation. The plasma density at the end of the ionization was $10^{-2}n_c$. The incident field strength was equivalent to $v_{osc}/c = 0.2$. (b) ω spectrum of the backscattered electric-field component E_y leaving the left-hand boundary, showing a narrow feature shifted by ω_{BG} [Eq. (2.1)]. (c) ω spectrum at the left-hand boundary of the incident electric-field component E_y for a 2D simulation. The plasma density at the end of the ionization was $4 \times 10^{-2}n_c$. The incident field strength was equivalent to $v_{osc}/c = 0.2$. (d) ω spectrum of the backscattered electric-field component E_y leaving the left-hand boundary showing a broad spectral feature in contrast with the spectrum of (b).

space-charge fields. Their phase-averaged guiding-center energy can increase in a stochastic fashion leading to hotter plasmas.

To investigate the importance of stochastic heating, a 2D simulation was carried out using a collimated beam and a density $n/n_c = 4 \times 10^{-4}$, too low for the parametric instabilities or refraction to occur. It was indeed found that at the end of the laser pulse, the plasma had a higher $T_\parallel$ than expected from the single-particle model (50 eV vs 2 eV in the 1D computations) [Figs. 10(c) and 10(d)]. Using a focused beam, electrons with a longitudinal drift velocity were generated at the edge of the plasma where the light rays make the largest angle. When the density was increased to $n/n_c = 0.1$, strong refraction of the beam was observed, leading to large phase front curvature and further heating of electrons. We note that since the experiments were carried out at low density, collisional effects are relatively unimportant. For high-density plasmas, however, collisional heating will become important as an additional heating mechanism.

C. Weibel instability

To explain the further increase with time of $T_\parallel$, we considered the effect of the isotropization of the transverse distributions through the Weibel instability. Although it can be shown that the obtained distribution functions are stable to electrostatic perturbations along the x direction using the Penrose criterion [38], they are unstable to electromagnetic perturbations. In Sec. IV B we found that the transverse distribution function in a space-charge-dominated plasma is much more filled in than the 1D ring distribution obtained in the single-particle regime. We will therefore use the expression for the maximum theoretical growth rate for the Weibel instability in a bi-Maxwellian plasma given by [38]

$$\gamma_{\text{Weibel}} = \left[\frac{8}{27\pi}\right]^{1/2} \omega_p \left[\frac{kT_\parallel}{mc^2}\right]^{1/2} \frac{T_\parallel}{T_\perp} \left[\frac{T_\perp}{T_\parallel} - 1\right]^{3/2}.$$

(71)

The mode of the magnetic field with the maximum growth rate has a wave number k_B given by [38]

$$k_B = \frac{\sqrt{3}}{3} \frac{\omega_p}{c} \left[\frac{T_\perp}{T_\parallel} - 1\right]^{3/2}.$$

(72)

The electron-cyclotron frequency ω_{ce} corresponding to the saturation value of the magnetic field for the mode with the maximum growth rate is given by [39]

$$\omega_{ce} = 4 \left[\frac{3}{2}\right]^{1/2} \left[\frac{\gamma_{\text{Weibel}}}{\omega_p}\right]^2 \omega_p.$$

(73)

In Fig. 12(a) we show the theoretical Weibel instability growth rate [Eq. (71)] as a function of $T_\perp$. In calculating this growth rate we have used the assumption from the tunneling model that the transverse drift velocities (v_y, v_z) and the longitudinal drift velocity $v_\parallel$ (and hence, $T_\parallel$ and $T_\perp$) are related through
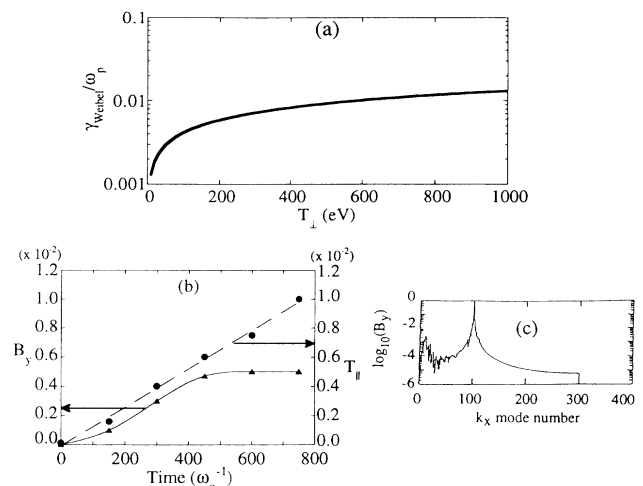

FIG. 12. (a) Theoretical Weibel instability growth rate as a function of $T_\perp$ for a tunnel-ionization-produced plasma. (b), (c) The time evolution of B_y and $T_\parallel$ starting after the end of the ionizing laser pulse and the k_x spectrum of B_y at $T = 1950\omega_0^{-1}$, from a 1D WAVE simulation. The plasma had a peak density $n = 5 \times 10^{-3} n_c$ and was created by a circularly polarized laser pulse with $v_{\text{osc}}/c = 0.2$ and a rise and fall time of $T = 500\omega_0^{-1}$. The feature with mode number around 100 in (c) corresponds to the wave number k_0 of the laser. The feature with mode number around 20, i.e., $k_B = 0.2k_0$, is due to the Weibel instability.

$$v_\parallel = \frac{v_y^2 + v_z^2}{2c}.$$

(74)

The isotropization of the electron-distribution functions due to the Weibel instability was isolated by running a 1D simulation with $n/n_c = 5 \times 10^{-3}$ and a short laser pulse $(1000\omega_0^{-1})$ to suppress parametric instabilities. Both the measured growth rate of the long-scale-length magnetic field characteristic of the Weibel instability and the wave number of the mode were in reasonable agreement with the theoretical predictions of $\gamma \approx 2 \times 10^{-3} \omega_0$ and $k_B \approx 0.2\omega_0/c$, respectively. The time evolution of the B_y component of the magnetic field and of $T_\parallel$ are shown in Fig. 12(b), and the k spectrum of B_y is shown in Fig. 12(b). It can be seen from Fig. 12(b) that temperature isotropization occurred over a slower time scale roughly given by $\tau \approx (\pi/2\omega_{ce})$, where ω_{ce} is given by Eq. (73). Using the theoretical growth rate for our experimental parameters we find that the Weibel instability will completely isotropize the electrons in roughly 75 ps (180 ps) for circular (linear) polarization. This is consistent with the observed broadening of the SCS spectrum [Fig. 5(b)] discussed earlier (Sec. III B). Although the simulations discussed here were carried out with a circularly polarized beam, similar effects occur with a linearly polarized beam.

V. CONCLUSION

The properties of tunnel-ionized plasmas have been studied through experiments and particle simulations. Odd-harmonic emission characteristic of stepwise tunnel ionization and density clamping due to ionization-

induced refraction were observed. Qualitative evidence for plasma temperature control by varying the laser polarization was obtained through measurements of the SCS instability spectra and x-ray emission. Furthermore, longitudinal temperatures were higher than those expected from a single-particle model. Simulations indicated that stochastic heating and the Weibel instability play an important role in plasma heating and isotropization. The maximum obtainable density was found to be limited by ionization-induced refraction. A simple scaling law for the density clamping was derived by blending concepts from the paraxial-ray approximation with Gaussian optics and was confirmed by simulations.

ACKNOWLEDGMENTS

*Present address: Lawrence Berkeley Laboratory, Berkeley, CA 94720.

†Permanent address: Institute for Plasma Research, Bhat Gandhinadar 382 424, India.

[1] L. V. Keldysh, Zh. Eksp. Teor. Fiz. 47, 1945 (1965) [Sov. Phys.—JETP 20, 1307 (1965)].

[2] L. D. Landau and E. M. Lifshitz, *Quantum Mechanics*, 3rd ed. (Pergamon, London, 1978).

[3] L. D. Landau and E. M. Lifshitz, *The Classical Theory of Fields* (Pergamon, Oxford, 1962).

[4] P. K. Kaw and R. M. Kulsrud, Phys. Fluids 16, 321 (1973).

[5] P. B. Corkum et al., Phys. Rev. Lett. 62, 1259 (1989).

[6] N. H. Burnett and G. D. Enright, IEEE J. Quantum Electron. 26, 1797 (1990).

[7] F. Yergeau et al., J. Phys. B 20, 723 (1987).

[8] M. D. Perry et al., Phys. Rev. Lett. 60, 1270 (1988).

[9] A. l'Huillier et al., Phys. Rev. A 27, 2503 (1983).

[10] P. Amendt et al., Phys. Rev. Lett. 66, 2589 (1991).

[11] T. Tajima and J. M. Dawson, Phys. Rev. Lett. 43, 267 (1979).

[12] C. Joshi et al., Nature (London) 311, 525 (1984).

[13] W. P. Leemans et al. (unpublished).

[14] W. P. Leemans et al., Phys. Rev. Lett. 68, 321 (1992).

[15] D. W. Forslund et al., Phys. Rev. Lett. 54, 558 (1985); J. N. Bardsley et al., Phys. Rev. A 40, 3823 (1989); J. T. Mendonça, J. Plasma Phys. 34, 115 (1985).

[16] E. S. Weibel, Phys. Rev. Lett. 2, 83 (1959).

[17] M. C. Downer et al., Phys. Rev. Lett. 65, 2832 (1990).

[18] M. N. Rosenbluth, Phys. Rev. Lett. 29, 565 (1972).

[19] W. P. Leemans et al. (unpublished).

[20] J. F. Drake et al., Phys. Fluids 17, 778 (1974).

[21] W. P. Leemans et al., *Report of the Workshop on Laser Plasma Simulations, Orsay, 1990*, edited by M. G. Haines (CECAM, Orsay, France, 1990), pp. 33–43; R. Rankin et al., Opt. Lett. 16, 835 (1991).

[22] F. Brunel, J. Opt. Soc. Am. 7, 521 (1990).

[23] J. F. Ward and G. H. C. New, Phys. Rev. 185, 57 (1969).

[24] P. Sprangle et al., Phys. Rev. A 41, 4463 (1990).

[25] *CRC Handbook of Laser Science and Technology*, edited by M. J. Weber (CRC, Cleveland, 1982).

[26] H. J. Lehmeier et al., Opt. Commun. 56, 67 (1985).

[27] W. B. Mori and C. B. Decker (unpublished).

[28] J. Meyer and Y. Zhu, Phys. Fluids 30, 890 (1987).

[29] C. J. Walsh et al., Phys. Rev. Lett. 53, 1445 (1984).

[30] W. P. Leemans et al., Phys. Rev. Lett. 67, 1434 (1991).

[31] J. Sheffield, *Plasma Scattering of Electromagnetic Radiation* (Academic, New York, 1975).

[32] D. W. Forslund et al., Phys. Fluids 18, 1002 (1975).

[33] J. Bernard et al., Phys. Rev. A 39, 2549 (1989).

[34] M. N. Rosenbluth and C. S. Liu, Phys. Rev. Lett. 29, 701 (1972).

[35] C. B. Darrow et al., Phys. Rev. Lett. 56, 2629 (1986).

[36] I. P. Shkarofsky et al., *The Particle Kinetics of the Plasmas* (Addison-Wesley, Reading, MA, 1966).

[37] J. M. Wallace et al., Phys. Fluids 3, 2337 (1991).

[38] N. A. Krall and A. W. Trivelpiece, *Principles of Plasma Physics* (McGraw-Hill, New York, 1973).

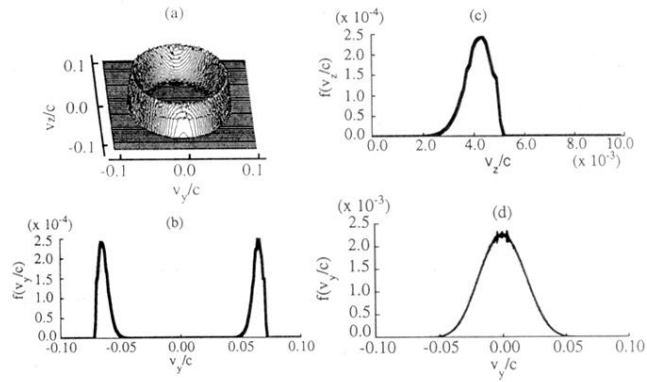[39] K. Estabrook, Phys. Rev. Lett. 41, 1808 (1978).

FIG. 2. (a) The calculated (single-particle regime) 2D transverse-electron drift-velocity distribution $f(v_y, v_z)$ produced by a circularly polarized laser with an intensity of 1.2×10^{14} W/cm^2, in argon gas. (b) Slice through (a) at $v_z = 0$, showing a major radius of $0.065c$ and a minor radius of $0.006c$. (c) Associated longitudinal drift-velocity distribution (10 times expanded velocity scale). (d) Calculated (single-particle regime) transverse-electron drift-velocity distribution $f(v_y)$ produced by a linear polarized laser with an intensity of 1.2×10^{14} W/cm^2, in argon gas. This quasi-Maxwellian distribution has a temperature $T_\perp$ of about 150 eV. The longitudinal drift-velocity distribution (not shown) is also quasi-Maxwellian with $T_\parallel \ll 1$ eV.
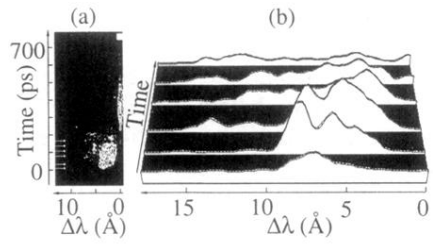
FIG. 5. (a) Streak camera image of the Thomson-scattered probe beam in a hydrogen plasma. The fill pressure was 1.1 Torr. Although not shown here, there was no blue shifted spectral feature visible in the original data. The white bar at the top indicates the location of a $100\times$ attenuator for SBS. (b) Line outs of the streak data taken along the direction of the arrows in (a).
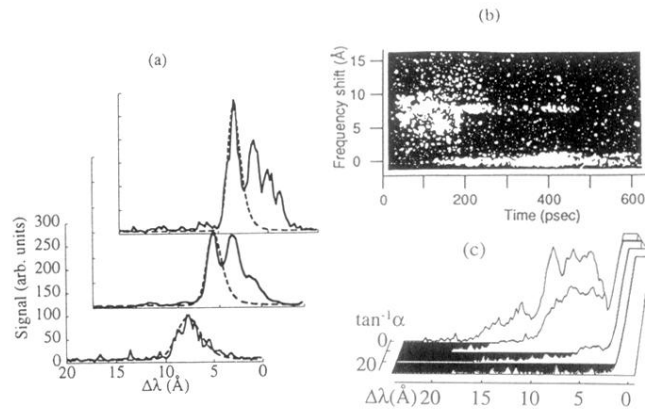
FIG. 6. (a) Plot of first three line outs and fitted curves; (b) time-resolved frequency spectrum of $2\mathbf{k_0}$ electron-density fluctuations. Wavelength shift increases upwards and time increases to the right. The feature near zero shift is from ion waves. The electron plasma wave feature due to SCS ranges from 0–15 Å. The feature at around 8 Å is the beat wave response of the plasma. The laser beam contained both a 10.3 and a 10.6-μm line, requiring a resonant density of 8×10^{15} cm^{-3}. (c) Time integrated streak camera images of the Thomson-scattered probe beam in hydrogen plasmas (fill pressure of 1.1 Torr) for different degrees of ellipticity α of the laser polarization ($\tan^{-1} \alpha = 45$ for circular polarization).
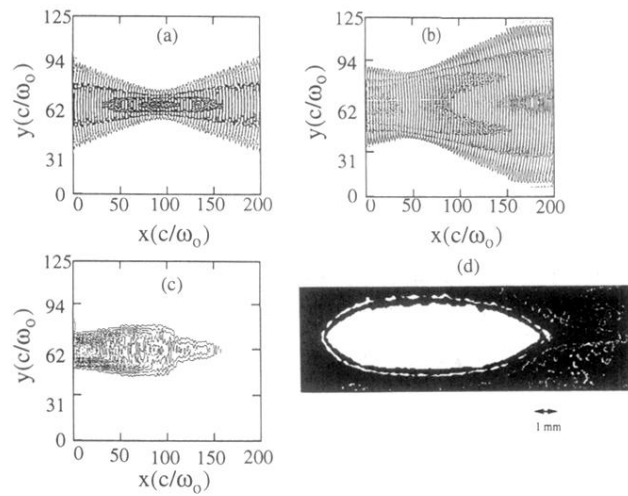
FIG. 9. (a) and (b) Calculated contour plots of E_z field and (c) of the plasma density from WAVE simulation at time step $T = 900\omega_0^{-1}$. The simulation box is $(200c/\omega_0 \times 125c/\omega_0)$. The incident laser field is launched from the left-hand boundary into vacuum in (a) and into a plasma with peak density $n = 0.1n_c$. In case (b) strong field refraction has occurred as seen from the E field peaking of axis at $x = 150c/\omega_0$ and the plane of highest intensity having moved backwards. Notice also in (c) how the location of the plasma is not centered on the box. (d) CCD camera image of the visible radiation given off by the plasma. The scale lengths in the experiment are different than in the simulation.